



# Spatial and temporal variability of the California Current identified from the synoptic monthly gridded World Ocean Database (WOD)



Peter C. Chu\*, Tetyana Margolina, DyAnna Rodriguez, Chenwu Fan, Leonid M. Ivanov

Department of Oceanography, Naval Postgraduate School, Monterey, CA 93943, United States

## ARTICLE INFO

### Keywords:

California Current  
Acceleration potential  
World Ocean Database (WOD)  
Synoptic monthly gridded WOD (SMG-WOD)  
Optimal spectral decomposition (OSD)  
Composite analysis  
Empirical Orthogonal Function (EOF)  
El Niño Modoki index (EMI), Multivariate  
ENSO index (MEI), Pacific Decadal Oscillation  
(PDO), North Pacific Gyre Oscillation (NPGO),  
Southern Oscillation Index (SOI)

## ABSTRACT

The synoptic monthly gridded (SMG) world ocean database (WOD) were constructed with  $1^\circ \times 1^\circ$  horizontal resolution and 28 standard vertical levels from the surface to 3000 m deep using the optimal spectral decomposition technique. Monthly acceleration potential (AP) relative to 1000-dbar is calculated for the isopycnal surface  $26.4 \text{ kg m}^{-3}$  from January 1960 to December 2014 to investigate the spatial and temporal variability of the California Current. A composite analysis was conducted to obtain the total-time mean AP field and the climatological monthly mean AP variability, which is two orders of magnitude smaller than the total-time mean. Residual data were used to examine interannual variations of the AP field. An empirical orthogonal function (EOF) analysis was conducted to analyze the AP anomaly data. The EOF-1 (40% variance) represents strengthening/weakening of the North Pacific Gyre and California Current. EOF-2 (20% variance) represents onshore/offshore geostrophic flow. The first principal component was negatively correlated with the PDO; the second principal component was negatively correlated with both the PDO and ENSO, which implied that the AP anomaly contains climate variability signals.

## 1. Introduction

The California Current System (CCS) has two major characteristics. First, the California Current (CC) transports subpolar waters southward, cooling and freshening coastal waters. Second, prevailing northwesterly winds associated with the North Pacific High (Taylor et al., 2008) cause extensive upwelling of colder, saline sub-surface waters at the coast through Ekman pumping and offshore transport. The upwelling further cools coastal waters.

The CCS has been studied extensively from many hydrographic surveys in the region from the equator to  $55^\circ\text{N}$  and from the west coast of North America to  $165^\circ\text{W}$ . Major experiments and surveys include the California Cooperative Oceanic Fisheries Investigations (CalCOFI) (e.g. Reid et al., 1958; Wyllie, 1966; Hickey, 1979; Chelton, 1984; Lynn and Simpson, 1987; Collins et al., 1996), the Coastal Ocean Dynamics Experiment (CODE) (e.g. Kosro, 1987), the Coastal Transition Zone (CTZ) Experiment (e.g. Paduan and Niiler, 1990; Brink and Cowles, 1991; Kosro et al., 1991), R/V *Point Sur* and World Ocean Circulation Experiment (WOCE) cruises (e.g. Castro et al., 2001), Argo and other individual surveys (e.g. Kosro and Huyer, 1986; Steger et al., 1998; Collins et al., 2000). A common practice is to calculate geostrophic velocity relative to a certain reference level (e.g. 1000-dbar by Castro et al., 2001) from observational temperature and salinity profiles to

represent the CCS. Temporal and spatial variability of the CCS has been identified from the geostrophic currents for the area and time period that the ( $T, S$ ) data were collected.

The CCS is influenced by the tropical Pacific climate systems. The two most energetic climate modes of interannual variability in the Equatorial Pacific Ocean are the canonical El Niño and pseudo-El Niño (or sometimes called central Pacific El Niño, or El Niño Modoki). The canonical El Niño event is characterized by weakening of trade winds and in turn warming in the eastern Pacific. The pseudo-El Niño is characterized by warming in the central equatorial Pacific and cooling in the eastern and western equatorial Pacific (Ashok et al., 2007; Weng et al., 2007).

Effects of canonical El Niño events on the CCS have been investigated by numerous studies especially after the strong 1997–1998 El Niño event. Two main mechanisms have been recognized: (1) atmospheric forcing through weakening of the upwelling favorable northwesterly winds; and (2) oceanic forcing through poleward propagating thermocline depth disturbances from the equatorial Pacific by coastally-trapped Kelvin waves (see, for example, Jacox et al., 2016). While different in nature and unknown in their relative contributions, both forcing mechanisms result in warming of upper layers, reducing biological productivity, and formation of nutrient depleted waters. However, the effects of pseudo-El Niño on the CCS have not been

\* Corresponding author.

E-mail address: [pcchu@nps.edu](mailto:pcchu@nps.edu) (P.C. Chu).

investigated.

This paper uses a synoptic monthly gridded ( $1^\circ \times 1^\circ$ ) world ocean database (SMG-WOD) for January 1960 to December 2014 (Chu and Fan, 2016) for the area [ $165^\circ\text{W}$ – $105^\circ\text{W}$ ,  $5^\circ$ – $55^\circ\text{N}$ ] to investigate long-term spatial and temporal variability focusing on the CCS in the Eastern North Pacific. The California Undercurrent is not well resolved by the  $1^\circ \times 1^\circ$  grid and is therefore not discussed. The paper is organized as follows: Section 2 describes data and methods; Section 3 shows the results and discusses mean patterns, as well as temporal and spatial variability of AP anomaly and its connection to the climate variability.; and Section 4 presents conclusions.

## 2. Data and methods

### 2.1. SMG-WOD database

The NOAA National Oceanographic Data Center (NODC), now a part of the National Centers for Environmental Information (NCEI), collects available ocean profile data into the World Ocean Database (WOD) (see the website: [https://www.nodc.noaa.gov/OC5/WOD/pr\\_wod.html](https://www.nodc.noaa.gov/OC5/WOD/pr_wod.html)), which has been widely used to create climatological and regional oceanographic products (Boyer et al., 2013). Recently, the optimal spectral decomposition (OSD) method (Chu et al., 2003a, 2003b, 2004, 2015, 2016) (see Appendix A), developed at the Naval Postgraduate School, was used to create SMG-WOD with 28 vertical levels, which coincide with those of the World Ocean Atlas (WOA09), from January 1945 to December 2014 (Chu and Fan, 2017). The SMG-WOD database is stored at NCEI for public use (see website: <http://data.nodc.noaa.gov/cgi-bin/iso?id=gov.noaa.nodc:0140938>). The data used to construct the SMG-WOD dataset are mostly from CTDs, XBTs, and profiling floats. The number of observations and spatial coverage varied significantly from year to year (Fig. 1). This created a challenge when creating synoptic monthly fields, especially for salinity. To minimize a possible bias caused by the uneven time-space distribution of raw data, only the data for 1960–2014 were used in this paper.

### 2.2. Error estimation

The OSD analysis error is the combination of the spectral error  $\varepsilon_K(\mathbf{r}_n)$  and observational error  $\varepsilon_o(\mathbf{r}_n)$  [see (A3) in Appendix A]. The observational error is usually the summation of human and instrumentation errors. The WOD and GTSPP profile data have been quality controlled to minimize the human error. Thus, the observational error  $\varepsilon_o(\mathbf{r}_n)$  can be treated as instrumentation error, which is much smaller than the spectral error  $\varepsilon_K(\mathbf{r}_n)$  [see (A3) and (A4)]

$$\varepsilon_a(\mathbf{r}_n) \approx \varepsilon_K(\mathbf{r}_n) = s_K(\mathbf{r}_n) - D(\mathbf{r}_n), \quad s_K(\mathbf{r}_n) \equiv \sum_{k=1}^K a_k \phi_k(\mathbf{r}_n) \quad (1)$$

where  $D(\mathbf{r}_n)$  is the observational innovation (at the grid points) depending only on the location of the observation [see (A5)];  $\phi_k(\mathbf{r}_n)$  and  $a_k$  ( $k = 1, 2, \dots, K$ ) are basis functions and spectral coefficients. The basis functions  $\phi_k(\mathbf{r}_n)$  are the eigenfunctions of the Laplacian operator, which are determined by the ocean topography. The spectral coefficients ( $a_k$ ) are calculated from the observational data by solving the linear algebraic Eq. (A7).

The analysis error of the SMG-WOD dataset is calculated for temperature and salinity at each time instance (i.e. monthly) and grid point. The root-mean square (RMS) errors of temperature and salinity (1960–2014) are computed for the three depths (0 m, 100 m, 500 m) and six zones of the CCS domain and (Fig. 2). The RMS error of temperature at all depths is less than  $0.14^\circ\text{C}$  south of  $30^\circ\text{N}$  and does not exceed  $0.24^\circ\text{C}$  north of  $30^\circ\text{N}$ . On the other hand, the RMS error of salinity is larger than  $0.03$  psu south of  $30^\circ\text{N}$  and does not exceed  $0.03$  psu north of  $30^\circ\text{N}$ . The different error distributions for temperature and salinity needs further investigation.

### 2.3. Acceleration potential

The SMG-WOD temperature and salinity gridded fields were used to calculate the monthly varying acceleration potential (AP),  $\psi$ , which is used to represent geostrophic flow on isentropic surfaces (Montgomery, 1937, cited by De Szoeke, 2000):

$$\psi = \int_{\delta_0}^{\delta} p d\delta + p_0 \delta_0, \quad (2a)$$

where

$$\delta(S, T, p) = \frac{1}{\rho(S, T, p)} - \frac{1}{\rho(35, 0, p)}, \quad (2b)$$

is the specific volume anomaly at pressure  $p$  with  $\delta_0$  being its value at the reference pressure ( $p_0$ ). The isopycnal surface  $\sigma_\theta = 26.4 \text{ kg/m}^3$  and  $p_0 = 1000 \text{ dbar}$  were chosen to represent the intermediate circulation in the CCS region. This isopycnal surface corresponds to the upper boundary of the North Pacific Intermediate Water (NPIW) [for example, You (2003) used the  $26.5 \text{ kg m}^{-3}$  neutral surface to approximate the layer above of the NPIW core], and is suitable to investigate the spatial distribution of the upper NPIW formed in the subarctic North Pacific (Yamanaka et al., 1998).

Due to the horizontal resolution of the SMG-WOD data ( $1^\circ \times 1^\circ$ ), the California Undercurrent and inshore Countercurrent are not well resolved by the calculated AP field. Note that we have also excluded the equatorial region, where the geostrophic approximation does not work well. The area to the north of  $55^\circ\text{N}$  has also been excluded because the isopycnal surface of  $26.4 \text{ kg m}^{-3}$  is shallow enough to outcrop in the northernmost regions.

### 2.4. Composite and EOF analyses

The composite analysis (Chu et al., 1997, 1998) decomposes a 4D variable  $\psi(\mathbf{r}_i, \tau_k, t_i)$  into seasonal and non-seasonal components. Here, the vectors  $\mathbf{r}_i$  represent locations on the 2D grid,  $i = 1, 2, \dots, I$ , where  $I$  is the total number of the grid points;  $\tau_k = 1960, 1961, \dots, 2014$  is the time sequence in years; and  $t_i = 1, 2, \dots, 12$  is the monthly sequence within a year. The climatological monthly means,  $\bar{\psi}(\mathbf{r}_i, t_i)$ , are calculated as multi-year averages of  $\psi(\mathbf{r}_i, \tau_k, t_i)$ :

$$\bar{\psi}(\mathbf{r}_i, t_i) = \frac{1}{K} \sum_{k=1}^K \psi(\mathbf{r}_i, \tau_k, t_i), \quad K = 55 \text{ (1960 to 2014)}. \quad (3)$$

The climatological annual mean,  $\bar{\bar{\psi}}(\mathbf{r}_i)$ , which is calculated as a total-time average of  $\psi(\mathbf{r}_i, \tau_k, t_i)$ :

$$\bar{\bar{\psi}}(\mathbf{r}_i) = \frac{1}{12} \sum_{l=1}^{12} \bar{\psi}(\mathbf{r}_i, t_l), \quad (4)$$

The climatological monthly anomalies,  $\tilde{\psi}(\mathbf{r}_i, t_i)$ , are calculated as deviations of climatological monthly means from the annual mean, and characterize the intra-annual variations of  $\psi(\mathbf{r}_i, \tau_k, t_i)$ :

$$\tilde{\psi}(\mathbf{r}_i, t_i) = \bar{\psi}(\mathbf{r}_i, t_i) - \bar{\bar{\psi}}(\mathbf{r}_i), \quad (5)$$

The synoptic monthly anomalies,  $\hat{\psi}(\mathbf{r}_i, \tau_k, t_i)$ , are calculated as deviations of synoptic monthly values from the climatological monthly means, and characterize the inter-annual (non-seasonal) variations of  $\psi(\mathbf{r}_i, \tau_k, t_i)$ :

$$\hat{\psi}(\mathbf{r}_i, \tau_k, t_i) = \psi(\mathbf{r}_i, \tau_k, t_i) - \bar{\psi}(\mathbf{r}_i, t_i) \equiv \psi(\mathbf{r}_i, \tau_k, t_i) - [\tilde{\psi}(\mathbf{r}_i, t_i) + \bar{\bar{\psi}}(\mathbf{r}_i)] \quad (6)$$

The synoptic monthly anomalies  $\hat{\psi}(\mathbf{r}_i, \tau_k, t_i)$ , were re-arranged into an  $I \times P$  matrix,  $\hat{\psi}(\mathbf{r}_i, \tilde{t}_p)$ ,  $p = 1, 2, \dots, P$ ,  $i = 1, 2, \dots, I$ . Here  $P = 660$  is the total number of months;  $I = 3188$  is the total number of grid points where the acceleration potential is defined. Empirical orthogonal function (EOF) analysis (Lorenz, 1956) of acceleration potential anomaly data was used to analyze the non-seasonal variability of the

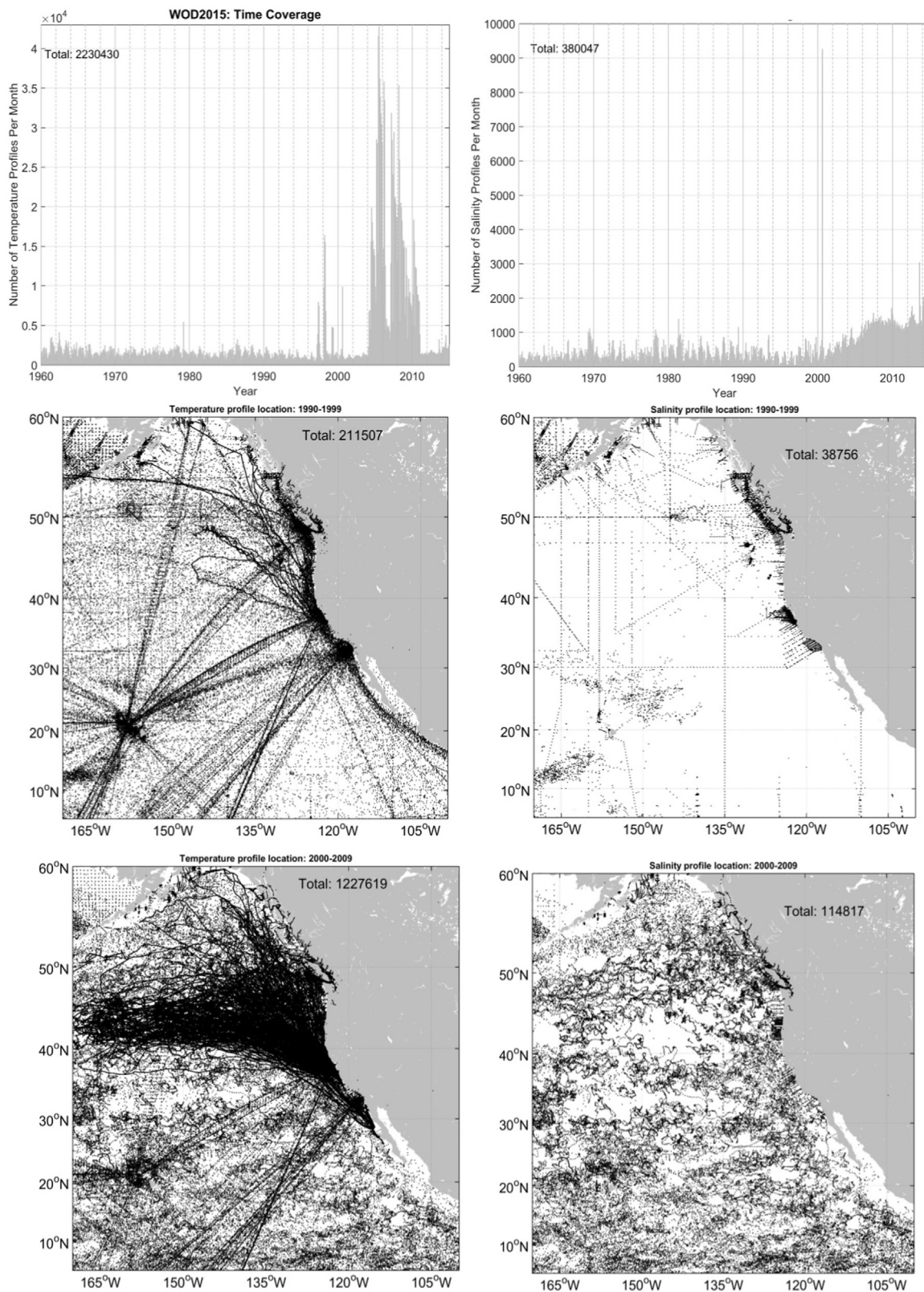


Fig. 1. Temporal (upper panels) and spatial (middle and lower panels) coverage for the SMG-WOD temperature (left-side panels) and salinity (right-side panels). The time-period is 1990–1999 for the middle panels and 2000–2009 for the lower panels.

intermediate circulation in the northeastern Pacific Ocean

$$\hat{\psi}(\mathbf{r}_i, \tilde{t}_p) = \sum_j PC_j(\tilde{t}_p) E_j(\mathbf{r}_i), \quad (7)$$

where  $E_j(\mathbf{r}_i)$  is the  $j$ th EOF mode (unit: J/kg); and  $PC_j(\tilde{t}_p)$  is the  $j$ th principal component (no unit) varying from  $-1$  to  $1$ . Statistical analysis was used to connect the temporal evolution of the principal component to known modes of climatological variability.

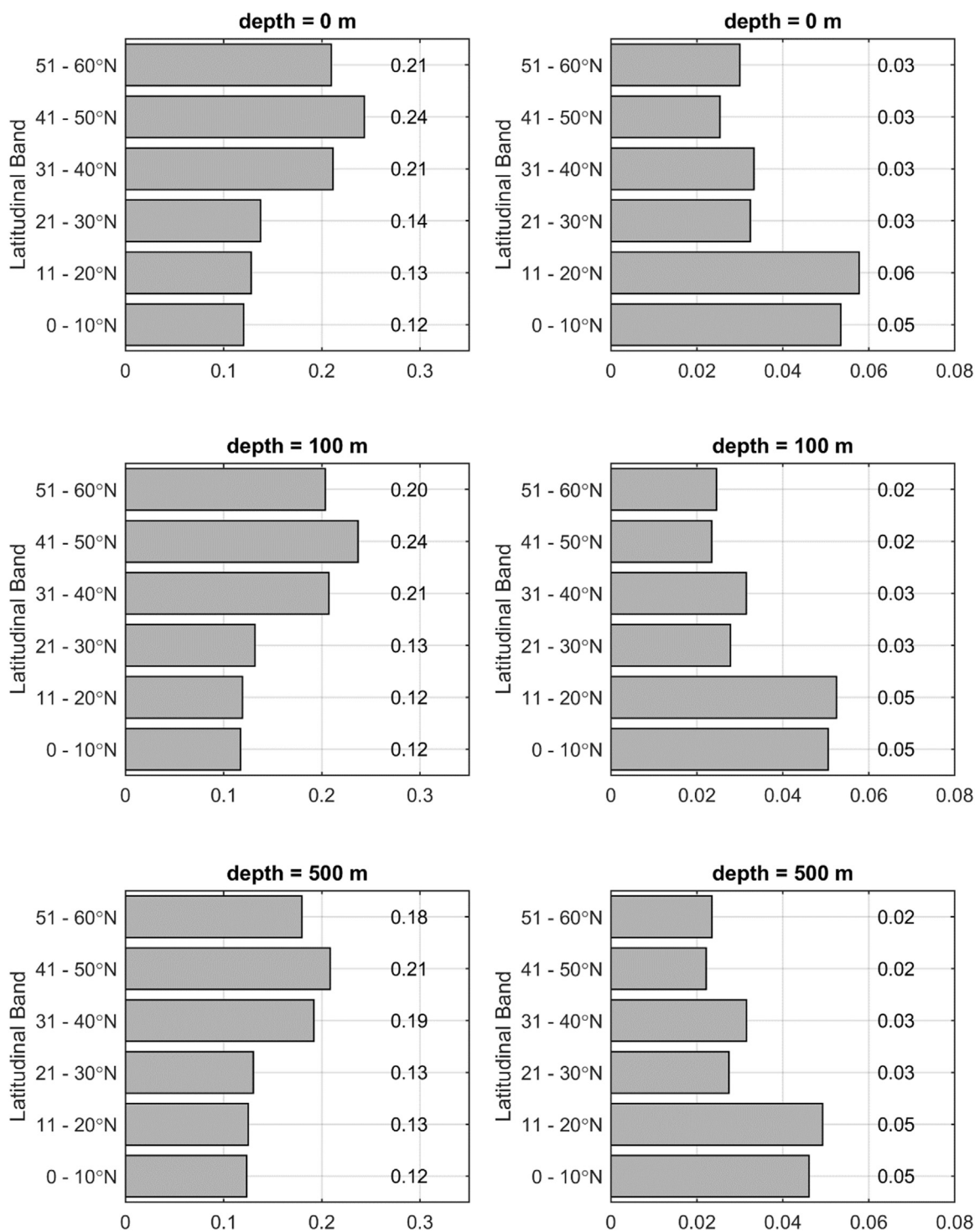


Fig. 2. Root Mean Square Error for temperature (left-side panels) and salinity (right-side panels) for latitudinal bands at three depths.

2.5. Climatological indices

Five climatological indices characterize climatological variability in the Northeast Pacific: Multivariate El Niño and Southern Oscillation Index (MEI), El Niño Modoki index (EMI), Southern Oscillation Index (SOI), Pacific Decadal Oscillation (PDO) index, and North Pacific Gyre Oscillation (NPGO) index. The time series of these indices for 1960–2014 are shown in Fig. 3.

The MEI (Fig. 3a) is a bi-monthly index calculated from six variables observed over the tropical Pacific: sea-level pressure, zonal and meridional components of the surface wind, sea surface temperature,

surface air temperature, and total cloudiness fraction of the sky (Wolter and Timlin, 2011). It is defined as the first un-rotated Principal Component (PC) of all six observed fields combined through normalizing the total variance of each field first, and then performing the extraction of the first PC on the co-variance matrix of the combined fields (see <http://www.esrl.noaa.gov/psd/enso/mei/> for detailed information). MEI was chosen for the present research because it is a composite indicator of ENSO for both atmosphere and ocean.

The EMI (Fig. 3b) represents the pseudo-El Niño (see [http://www.jamstec.go.jp/frcg/research/d1/iod/e/elnmodoki/about\\_elnm.html](http://www.jamstec.go.jp/frcg/research/d1/iod/e/elnmodoki/about_elnm.html)),

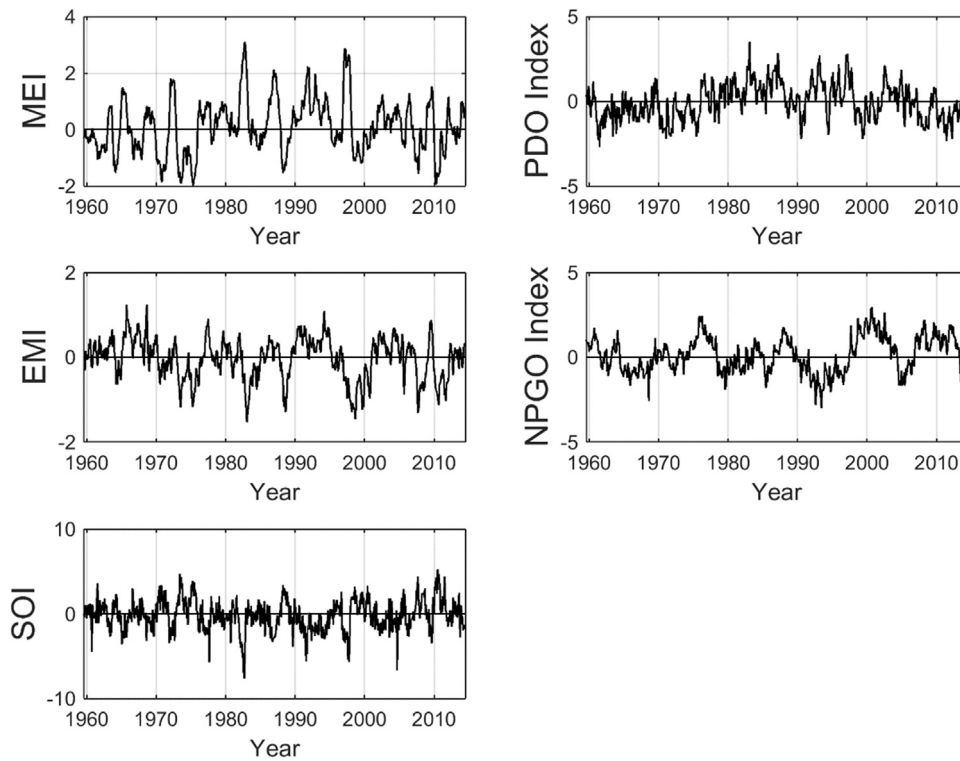


**Fig. 3.** Time series of (left column, top to bottom) Multivariate ENSO Index (MEI), El Niño Modoki index (EMI), Southern Oscillation Index (SOI); (right column, top to bottom) Pacific Decadal Oscillation (PDO) index, and North Pacific Gyre Oscillation (NPGO) index.

$$EMI = [SSTA]_A - 0.5*[SSTA]_B - 0.5*[SSTA]_C, \tag{8}$$

where the brackets represent the area-averaged sea surface temperature (SST) anomalies over the regions A (165°E–140°W, 10°S–10°N), B (110–70°W, 15°S–5°N), and C (125–145°E, 10°S–20°N), respectively

(Ashok et al., 2007). Fig. 3b shows the time series of EMI. While similar to the canonical El Niño, pseudo El Niño events are characterized by warm SST anomalies in the central rather than eastern Pacific. Pseudo El Niño events are known to have strong remote signatures in the Northeast Pacific Ocean (including the CCS) which differ from those

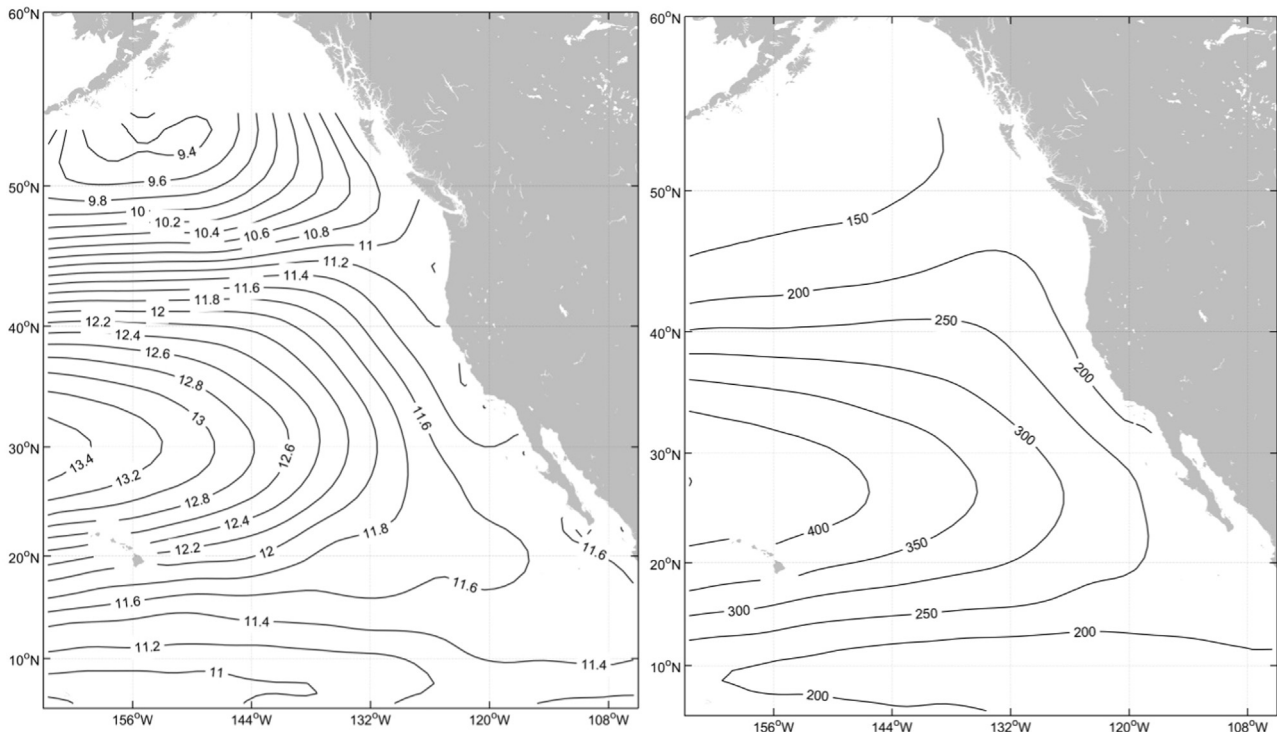


**Fig. 4.** Climatological annual mean of the acceleration potential ( $\bar{\psi}$ , unit:  $J kg^{-1}$ ) to represent the geostrophic flow on the  $26.4 kg m^{-3}$  isopycnal surface referenced to the 1000-dbar level (left) and corresponding pressure field in dbar (right). The contour interval is  $0.2 J kg^{-1}$  for acceleration potential and 50 dbar for pressure.

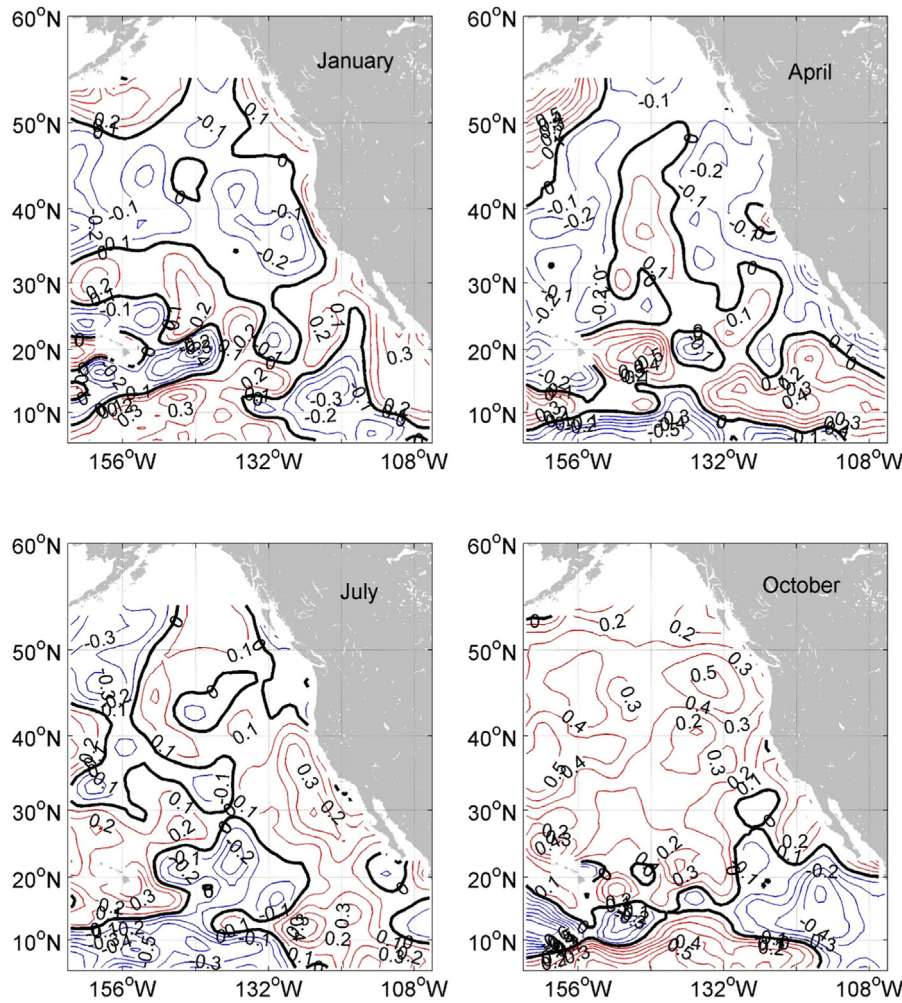


Fig. 5. Standardized climatological monthly mean anomaly of the acceleration potential on the  $26.4 \text{ kg m}^{-3}$  isopycnal surface referenced to the 1000-dbar level in January, April, July, and October. Red (blue) contours represent positive (negative) isosteres. Thick black contours are zero-values and the contour interval is 0.1.

associated with the canonical El Niño (Weng et al., 2007).

The PDO is the first leading mode of the decadal variability in the North Pacific, and is calculated as the coefficients of the first EOF of monthly SST anomalies for latitudes  $> 20^\circ\text{N}$  (<https://www.ncdc.noaa.gov/teleconnections/pdo/>; Zhang et al., 1997). Spatial patterns of cold and warm PDO phases are similar to those of ENSO but have an interdecadal period of approximately 10 years. Both PDO and El Niño are evident during winter seasons with increasing SST and precipitation due to the predominant southwesterly winds that create downwelling to reduce chlorophyll-a concentration at the coast in the CCS. The NPGO is the second leading mode of the decadal variability in the North Pacific (uncorrelated to PDO), and is calculated as the coefficients of the second EOF mode of the sea surface heights (SSH) anomalies (<http://www.o3d.org/npgo/>). Both decadal modes (NPGO and PDO) involve change of northwesterly winds. Increase in northwesterly winds enhances coastal upwelling and in turn increases Chl-a concentrations in the CCS. However, the NPGO is most pronounced in the sea surface salinity (SSS) while PDO is in the SST. The two modes are somewhat separated spatially in the CCS with PDO (NPGO) being more important northward (southward) of the  $38^\circ\text{N}$  latitude.

## 2.6. Correlation and time-frequency analysis

Preliminary analysis of the spectral content of the interannual/decadal variability of the AP monthly anomaly ( $\psi$ ) revealed a non-stationary signal at annual and shorter time scales. This near-annual

variability was synchronized approximately with most energetic 3–8 years components of the analyzed PCs. We hypothesize that the variability at the intra-annual scales is locked in phase with strong canonical El Niño events, which are known to begin in December and to last through the winter (for an extensive discussion see Neelin et al., 2000). To remove the intra-annual variability from the analyzed signals, we have filtered the first two PCs by applying the Daubechies 8-tap wavelet decomposition similar to the Mallat's approach (Mallat, 1989) and retaining five low-frequency components of each PC. We then applied the Morlet wavelet transformation (Torrence and Compo, 1998) to the filtered PCs to analyze the interannual/decadal variability of the AP monthly anomaly ( $\psi$ ). Although general wavelet methods have capability to analyze aperiodic signals, the Morlet wavelet has better resolution of narrowband signals and more straightforward interpretation of the frequency content, as compared to other types of wavelet kernels (see for example Ladd and Wilson, 1993).

The PCs of two leading EOFs of the AP monthly anomaly ( $\psi$ ) are correlated to the five indices of climate variability with p-values calculated at the 95% significance level. Since the correlated variables are presented by sequential time-series as opposed to random sampling, neighboring values are expected to be related within a time-period specified by the data. The approach of Sciremammanois (1979) was applied to calculate the degrees of freedom for the statistical estimates from the integral time scales. The degrees of freedom for the analyzed time-series with 660 months were estimated to be about 270–300 for different variables and climatological indices.

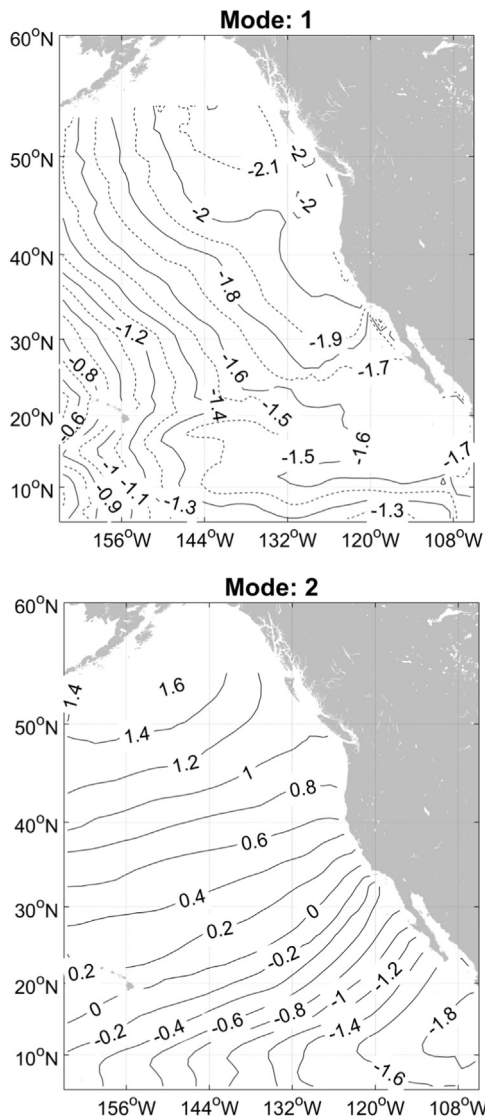


**Fig. 6.** First two EOFs of monthly anomaly of the acceleration potential ( $\hat{\psi}$ , J/kg) on the  $26.4 \text{ kg m}^{-3}$  isopycnal surface referenced to the 1000-dbar level. Solid isolines are plotted with a  $0.2 \text{ J kg}^{-1}$  step; dashed isolines are plotted at an additional  $0.1 \text{ J kg}^{-1}$  step.

### 3. Results and discussion

#### 3.1. Spatial-temporal variability of the acceleration potential

Fig. 4 shows the climatological annual mean AP field ( $\bar{\psi}(\mathbf{r}_i)$ ) (in  $\text{J kg}^{-1}$ ) (left panel) and the pressure (in dbar) (right panel). The climatological maximum (minimum) values of AP was  $\sim 13.5 \text{ J kg}^{-1}$  ( $\sim 9.3 \text{ J kg}^{-1}$ ). The corresponding geostrophic velocities were  $\sim 3.5 \text{ cm s}^{-1}$  in the region of the North Equatorial Countercurrent (NECC), and  $\sim 2.5 \text{ cm s}^{-1}$  in the North Pacific Current. The climatological annual circulation at the intermediate level agrees well with earlier studies, see for example the large scale AP field at a deeper isopycnal surface of  $26.9 \text{ kg m}^{-3}$ , derived by Castro et al. (2001) using the ( $T, S$ ) profile data from oceanographic cruises between 1970 and 1994. The circulation is characterized by three-gyres: cyclonic subpolar (Alaska) gyre (north of  $43^\circ\text{N}$ ), anticyclonic subtropical (North Pacific) gyre ( $12^\circ\text{N}$ – $43^\circ\text{N}$ ), and a weak cyclonic circulation in the tropical Pacific ( $5^\circ$ – $10^\circ\text{N}$ ). (As noted above, the cyclonic circulation along the West Coast of the U.S. is not resolved.) The northern and southern zonal branches of the anticyclonic North Pacific Gyre transport waters with

very characteristic and different signatures. The subarctic Pacific Water that feeds the CC from the north is characterized by low salinity, high oxygen, and high silicate. The water near the southeastern tip of the gyre (near  $120^\circ\text{W}$ ,  $20^\circ\text{N}$ ) from the CC is characterized by high salinity, low oxygen, and low silicate (Castro et al., 2001). The anticyclonic Tropical North Pacific Gyre transports southern waters to south of Baja California (Collins et al., 2000; Pierce et al., 2001).

The climatological monthly AP anomaly  $\tilde{\psi}(\mathbf{r}_i, t_i)$  in January, April, July, and October (not shown) represent the mean seasonal variability with patchiness, maximum absolute values of  $\sim 0.1 \text{ J kg}^{-1}$  in the tropical and northern regions, and were more than an order of magnitude smaller than the climatological annual mean  $\bar{\psi}(\mathbf{r}_i)$ . Larger seasonal variability and small-scale patchiness coincide in the tropical region (south of  $12^\circ\text{N}$ ). This is characteristic of the late spring to early winter development of the NECC, which responds to seasonally varying wind-forcing. geostrophic currents in the North Pacific Subtropical Gyre (i.e. large-scale CCS) have low seasonal variability. Note that low seasonal variability along the eastern boundary could be due to unresolved near-coast variability, e.g. seasonality in upwelling/downwelling and the spring transition events.

Fig. 5 shows the standardized climatological monthly anomalies, i.e. climatological monthly anomaly divided by its STD (Wilks, 2005). Removing the effect of spatially specific dispersion leads to the coherent structures of the seasonal variability. For example, the NECC strengthens in October and weakens in April. The CC weakens along the coast in winter. The Alaska Stream strengthens in April.

Empirical orthogonal function (EOF) analysis (Lorenz, 1956) was conducted using the acceleration potential anomaly data  $\hat{\psi}(\mathbf{r}_i, \tilde{t}_p)$  to analyze the non-seasonal variability. The first four EOFs contain 40%, 20%, 12%, and 6% of total variance, respectively, with the higher-order EOFs being inseparable. Here, the effort was concentrated on analyzing the first two EOF modes, which together captured 60% of the total non-seasonal variability. Fig. 6 shows the spatial patterns of first two EOFs of  $\hat{\psi}$ . Fig. 7 depicts the corresponding principal components.

The EOF-1 mode (Fig. 6a) shows a strengthening/weakening CC pattern with a south-southeastward (north-northwestward) flow during positive (negative) phase. This mode has a maximum (minimum) of  $-0.6 \text{ J kg}^{-1}$  ( $-2.1 \text{ J kg}^{-1}$ ) near  $20^\circ\text{N}$ ,  $162^\circ\text{W}$  (along the Eastern Boundary). For  $PC_1(\tilde{t}_p) > 0$ , the spatial variability of AP anomaly shows a weak south-southeastward flow except at  $10^\circ\text{N}$  where an eastward flow occurs to the east of  $144^\circ\text{W}$ . This pattern strengthens the North Pacific Subtropical Gyre and in turn enhances the CC. For  $PC_1(\tilde{t}_p) < 0$ , the horizontal variability of AP anomaly reverses, which weakens the North Pacific Subtropical Gyre and reduces the CC. The corresponding geostrophic velocities can vary as much as  $1$ – $2 \text{ cm s}^{-1}$ . For region [ $144$ – $120^\circ\text{W}$ ,  $30$ – $50^\circ\text{N}$ ] (called the CC upwelling cells by Chhak and Di Lorenzo (2007)), the condition [ $PC_1(\tilde{t}_p) > 0$ ] represents more horizontal entrainment of upper layer water from the north.

The EOF-2 mode (Fig. 6b) shows an offshore/onshore geostrophic flow pattern from  $10^\circ\text{N}$  to  $50^\circ\text{N}$  in the Northeast Pacific (except in the tropics) for positive principal components. The second principal component for 1945–2014,  $PC_2(\tilde{t}_p)$ , fluctuated between  $-1.8$  and  $1.6$  (Fig. 7b). The corresponding contribution of the second EOF to the total circulation at the intermediate level can be as high as  $1 \text{ cm s}^{-1}$  near  $10^\circ\text{N}$  to  $15^\circ\text{N}$ ,  $132^\circ\text{W}$ . In its positive (negative) phase, the circulation patterns of the second EOF mode strengthens (weakens) the offshore transport in the intermediate layer of the CCS. The depth of the  $24.6 \text{ kg m}^{-3}$  layer is 100 m close to the shore and deepens toward the ocean interior.

Strong spikes much higher than the rest of the PCs exist such as for  $PC_1$  in April 1986, September 1987, and May 1989 (Fig. 7). These spikes appear to be only one time step (i.e. one month). One may question non-realistic data for these dates (outliers, and/or interpolation issues due to a lack of data points, or some other issue that would cause the acceleration potential to be very different at these times than for adjacent months). Fig. 8 shows the acceleration potential ( $\psi$ ) for

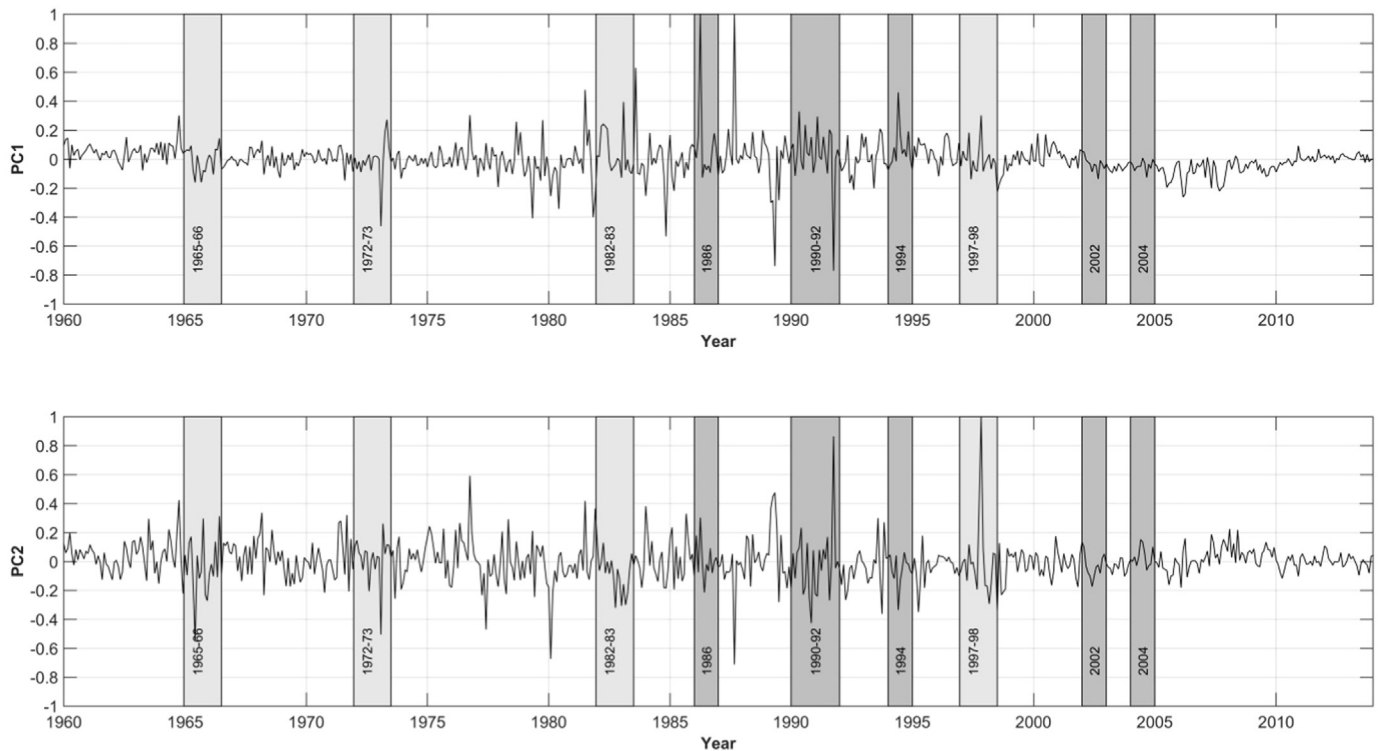


**Fig. 7.** First two PCs of monthly anomaly of the acceleration potential ( $\hat{\psi}$ ) on the  $26.4 \text{ kg m}^{-3}$  isopycnal surface referenced to 1000-dbar surface. Shaded areas in the upper and lower panels correspond to known El Niño Modoki (light-gray areas) and regular El Niño (dark-gray areas) events.

three consecutive months with sharp spikes of  $PC_1$  in the central panels. For April 1986 (Fig. 8, upper central panel), the circulation patterns are quite similar among the three consecutive months with three-gyre structure: cyclonic subpolar (Alaska) gyre (north of  $43^\circ\text{N}$ ), anticyclonic subtropical (North Pacific) gyre ( $12^\circ\text{N}$ – $43^\circ\text{N}$ ), and a weak cyclonic circulation in the tropical Pacific ( $5^\circ$ – $10^\circ\text{N}$ ). However, an additional cyclonic gyre strengthened and expanded westward from March to April 1986 west of Baja California at  $20^\circ\text{N}$ – $35^\circ\text{N}$ , and disappeared in May 1986. For September 1987 (Fig. 8, middle), the subpolar gyre disappears and in May 1989 (Fig. 8, lower), the subtropical and subpolar gyres weaken. Such sudden changes may not be realistic and need further investigation.

### 3.2. Time-frequency analysis

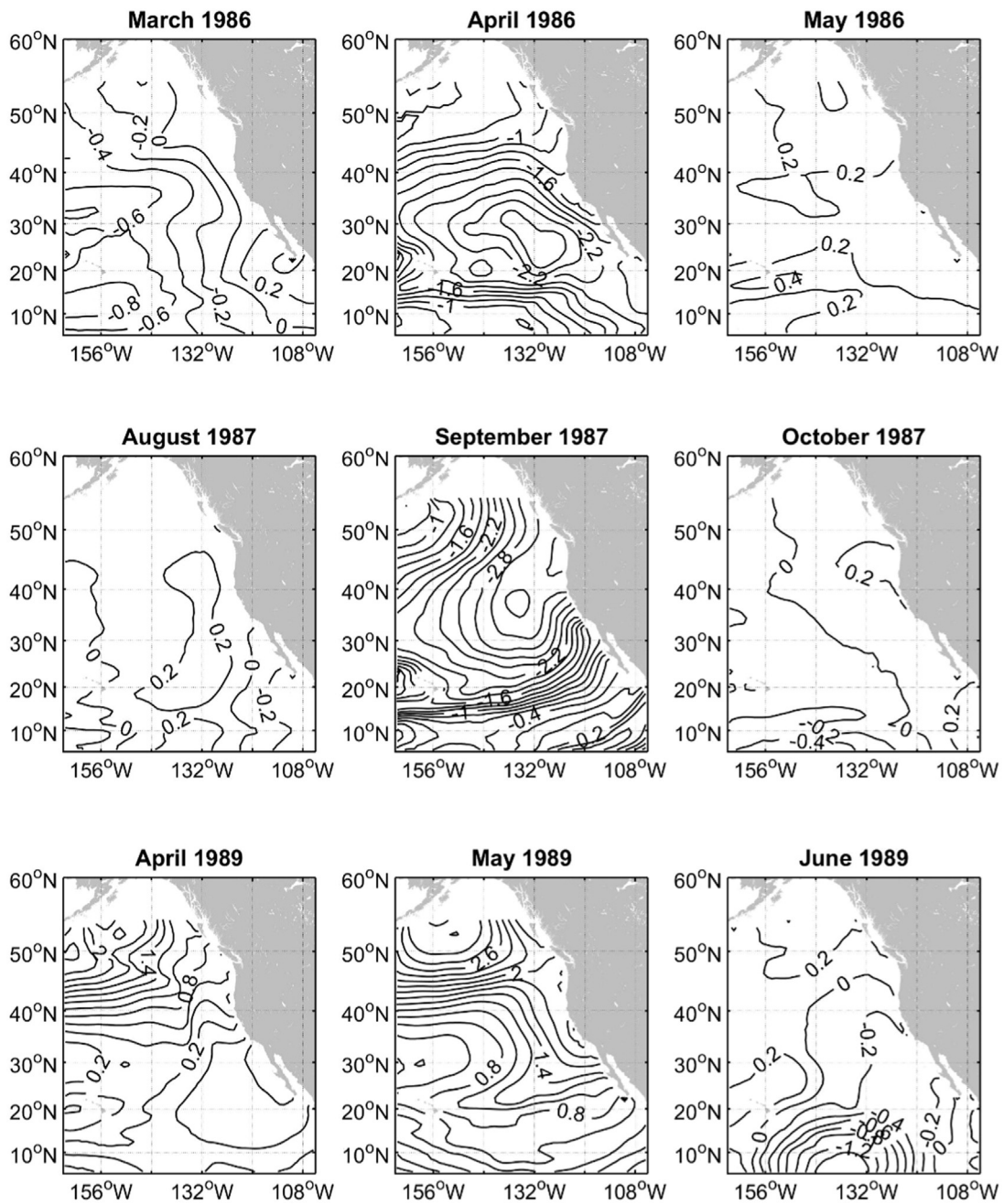
Fig. 9a and b show the power spectra of the Morlet wavelets of the first two PCs of monthly anomaly of the acceleration potential ( $\hat{\psi}$ ). The dashed white curves in each figure represent the wavelet cones of influence (COIs). Signal intensity is weak in the areas under COIs due to zero-padding. The vertical axes are labeled in Fourier periods (in years) corresponding to the wavelet scales (not shown). The 95% significance contours are shown as white solid curves. Interested readers are referred to Torrence and Compo for detailed information on wavelet theory and technique. Time varying scale-averaged (3–7 year period) power of  $PC_1$  and  $PC_2$  correspond approximately to ENSO (Fig. 9c). Wavelet power spectra of  $PC_1$  and  $PC_2$  averaged over the time-period 1960–2014 (Fig. 9d) show evident complex non-seasonal components (period of 2 years and longer) of the AP field. Leading harmonics and shifts of energy in both time and frequency domains are described below.

The main harmonics of  $PC_1$  were between 3 and 8 years, roughly corresponding to the canonical El Niño, and between 12 and 20 years, mainly related to decadal variability (Fig. 9d, solid black curve). The two spectral peaks were wide and contained several local maxima. As

shown in Fig. 9a, these peaks occurred during different time-periods: the main peak corresponds to roughly 1975–1993 and is represented by an energy ridge ( $> 40 \text{ J}^2 \text{ kg}^{-2}$ ) which changed period from 7 to 4 years between 1978 and 1991. Between 1985 and 2003, a prevailing harmonic occurred at periods of about 7 years.

From Fig. 9c, the variability at canonical ENSO frequencies was modulated strongly at multi-decadal scales, with two significant regime shifts in  $PC_1$ , in the mid-1970s and 1995. The period between the two shifts was characterized by highly energetic variability at the intermediate depths corresponding to ENSO. The mid-1970s shift from the PDO “cool” phase (pre mid-1970s) to the PDO “warm” phase has been found for the variability at the ocean surface (Bond et al., 2003; Chhak et al., 2007), and the CCS upwelling cells (Chhak and Lorenzo, 2007). However, stochastic forcing at scales not necessarily associated with PDO cause the shift in the Northeast Pacific ecosystem in late 1990 (Bond et al., 2003). The data don’t resolve whether the later shift observed in the non-seasonal variability of the intermediate layer of the Northeast Pacific is the same as that studied by Bond et al. (2003), which was based on the surface oceanographic conditions and atmospheric patterns.

Several regime shifts are also evident in the time-frequency domain for  $PC_2$  (Fig. 9b, and the black dotted line in Fig. 9c), as well as two frequency peaks in the global wavelet power spectrum (Fig. 9d). Unlike the wide peaks of  $PC_1$ , the most energetic frequency bands of  $PC_2$  were rather narrow, and corresponded to periods between 3 and 4 years, and 9–14 years (decadal scales). The 3–4 year harmonic was modulated by 15–20 year oscillations. The time-period between 1960 and the late 1970s was characterized by the narrowband (4-year period) maximum in the late 1960s. The second maximum was observed in 1985–1990, was more energetic, and occupied a wider band from 4 to 2.5 year period. Similar to  $PC_1$ , the period after 2000 was characterized by rather low energy. The second main harmonic of  $PC_2$  was represented by robust near-decadal oscillations, decreasing from a period of 12 years in 1970s to a period of 10 years in 2000s.



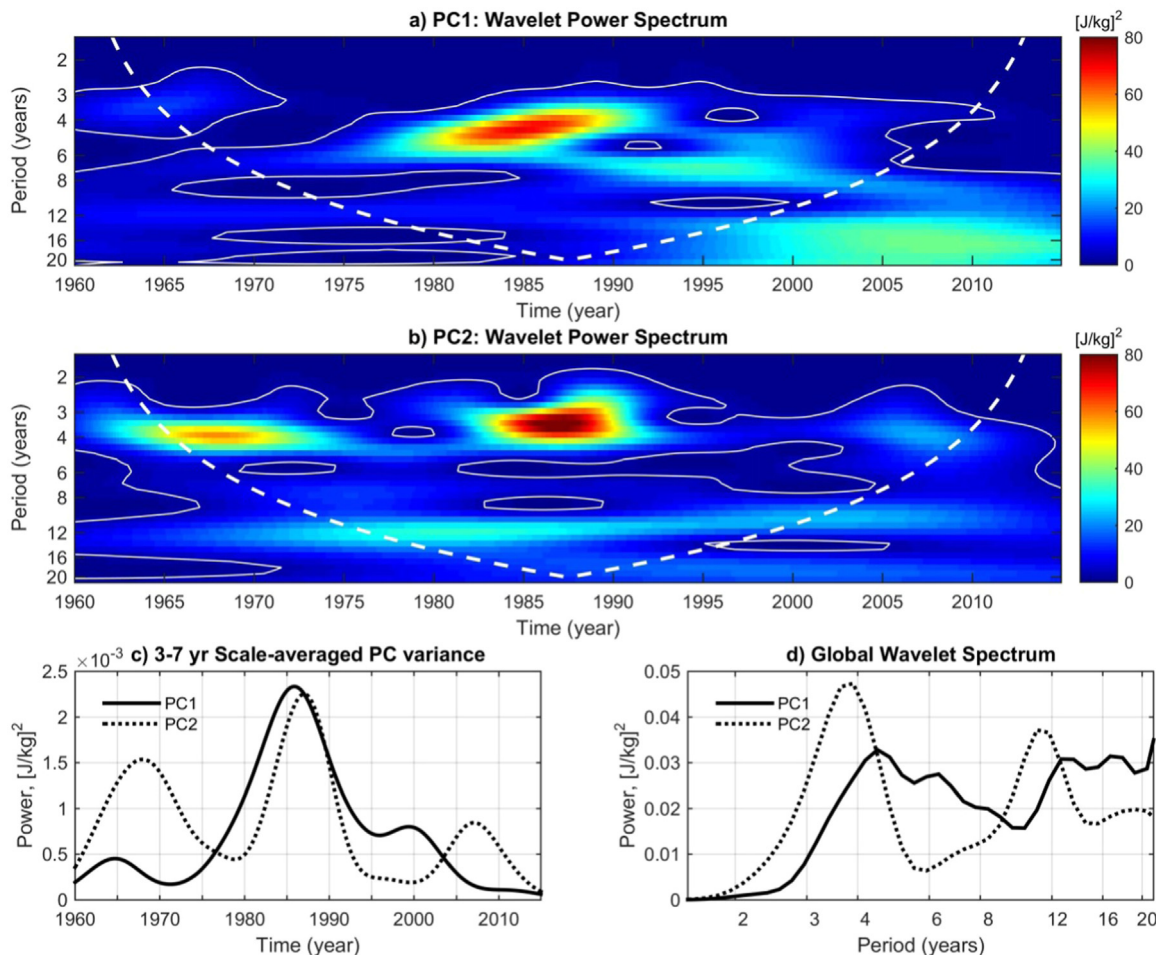


**Fig. 9.** Morlet wavelet transform of the first two filtered PCs of monthly anomaly of the acceleration potential ( $\hat{\psi}$ ) on the  $26.4 \text{ kg m}^{-3}$  isopycnal surface referenced to 1000-dbar surface: (a) and (b) are the wavelet power spectrum distributions for filtered PC1 and PC2, respectively. The white dashed lines are the wavelet cones of influence (COI). (c) is the PC variance averaged over the 3–7 year periods. (d) is the global wavelet power spectrum.

#### 4. Conclusions

This is the first observational study to investigate the spatial and temporal (seasonal/interannual/decadal) variability of the CCS system as represented by the acceleration potential and its relationship to the large-scale climatological indices such as the EMI and PDO using a recently developed SMG-WOD (T, S) dataset. Unlike many other studies, the focus of this paper is on the intermediate layer of the ocean, between 100 and 400 m, and its connection to the non-seasonal variability at the ocean surface. The composite, EOF, wavelet, and correlation analyses were used.

The total-time mean acceleration potential field is identified as two major gyres: the cyclonic Alaska Gyre (to the north of  $43^\circ\text{N}$ ), anticyclonic North Pacific Subtropical Gyre ( $12^\circ\text{N}$ – $43^\circ\text{N}$ ), as well as a weak cyclonic circulation in the tropical region ( $0^\circ$ – $12^\circ\text{N}$ ). Such a pattern agrees well with earlier studies (e.g. Castro et al., 2001; Kawabe and Fujio, 2010). Weak seasonal variability of the acceleration potential was identified but the monthly anomaly was an order of magnitude smaller than the climatological time mean.

An EOF analysis was conducted to analyze the monthly anomaly of the acceleration potential. The EOF-1 (40% variance) represents

#### Appendix A. Optimal Spectral Decomposition

A new ocean spectral data analysis/assimilation scheme, the optimal spectral decomposition (OSD), has been recently developed to analyze ocean observational data without background and observational error covariance matrices (Chu et al., 2015, 2016). Let the position vector  $\mathbf{r} = (x, y,$

strengthening/weakening of the North Pacific Gyre and in turn strengthening/weakening the California Current. The EOF-2 (20% variance) represented onshore/offshore geostrophic flow. The first principal component was negatively correlated to the PDO; the second principal component was negatively correlated to both PDO and MEI.

The spectral contents of the principal components of the non-seasonal variability of the acceleration potential in time-frequency domain were obtained using the Morlet wavelet transform. The connection between the temporal variability of climate indices and the CCS was identified. Strengthening/weakening of the California Currents (i.e., represented by EOF-1) is phase-locked to the ENSO event and seasonal cycles.

#### Acknowledgments

The Office of Naval Research, the Naval Oceanographic Office, and the Naval Postgraduate School supported this study. The authors thank Dr. L. Charles Sun at the NOAA/NCEI for his efforts on quality control of the SMG-WOD data and Emeritus Professor Curtis A. Collins (Guest Editor) for his scientific and editorial guidance, both of whom have greatly improved the quality of the manuscript.

$z$ ) be represented by  $\mathbf{r}_n$  ( $n = 1, 2, \dots, N$ ) at a grid point, and  $\mathbf{r}^{(m)}$  ( $m = 1, 2, \dots, M$ ) at an observational point. Here,  $N$  is the total number of the grid points, and  $M$  is the total number of observational points. Let an ocean variable be represented by a vector  $\mathbf{c}$  with background field ( $\mathbf{c}_b$ ) (at grid points) and observational data ( $\mathbf{c}_o$ ) (at observational points) can be represented by  $N$  and  $M$  dimensional vectors,

$$\mathbf{c}_b^T = [c_b(\mathbf{r}_1), c_b(\mathbf{r}_2), \dots, c_b(\mathbf{r}_N)], \quad \mathbf{c}_o^T = [c_o(\mathbf{r}^{(1)}), c_o(\mathbf{r}^{(2)}), \dots, c_o(\mathbf{r}^{(M)})], \quad (\text{A1})$$

where the superscript  $T$  means transpose. Let  $\mathbf{H} = [h_{mn}]$  be the  $M \times N$  linear observation operator matrix converting the background field  $\mathbf{c}_b$  (at the grid points,  $\mathbf{r}_n$ ) into “first guess observations” at the observational points  $\mathbf{r}^{(m)}$ . The  $M$ -dimensional vector

$$\mathbf{d} \equiv (\mathbf{c}_o - \mathbf{H}\mathbf{c}_b) = (d^{(1)}, d^{(2)}, \dots, d^{(M)}), \quad (\text{A2})$$

is defined as the innovation (also called the observational increment) at the observational points  $\mathbf{r}^{(m)}$ .

Existence of a lateral boundary ( $\Gamma$ ) for an ocean domain ( $\Omega$ ) provides a great opportunity to use a spectral method in ocean data analysis and assimilation through decomposing the variable anomaly at the grid points [ $c_a(\mathbf{r}_n) - c_b(\mathbf{r}_n)$ ] into the spectral form,

$$c_a(\mathbf{r}_n) - c_b(\mathbf{r}_n) = f_n s_K(\mathbf{r}_n), \quad s_K(\mathbf{r}_n) \equiv \sum_{k=1}^K a_k \phi_k(\mathbf{r}_n), \quad f_n \equiv \sum_{m=1}^M h_{nm} \quad (\text{A3})$$

where  $\{\phi_k\}$  are basis functions; and  $K$  is the mode truncation. The analysis error (i.e. analysis  $c_a$  versus “truth”  $c_t$ ) is given by

$$\begin{aligned} \varepsilon_a(\mathbf{r}_n) &= \varepsilon_K(\mathbf{r}_n) + \varepsilon_o(\mathbf{r}_n), \\ \varepsilon_K(\mathbf{r}_n) &= s_K(\mathbf{r}_n) - D(\mathbf{r}_n), \quad \varepsilon_o(\mathbf{r}_n) = c_o(\mathbf{r}_n) - c_t(\mathbf{r}_n) \end{aligned} \quad (\text{A4})$$

where  $D(\mathbf{r}_n)$  represents the observational innovation at the grid points,

$$D_n \equiv D(\mathbf{r}_n) = \frac{\sum_{m=1}^M h_{nm} d^{(m)}}{f_n} \quad (\text{A5})$$

$\varepsilon_K(\mathbf{r}_n)$  is the truncation error; and  $\varepsilon_o(\mathbf{r}_n)$  is the observational error.

The eigenvectors of the Laplace operator with the same lateral boundary condition of  $(c - c_b)$  can be used as the basis functions  $\{\phi_k\}$ . With the spectrum (A3), the representation of the relation between the observed and grid points has been changed from the  $M \times N$  background error covariance matrix  $\mathbf{B}$  (*a posteriori*) to the  $K \times N$  basis function matrix  $\Phi$  (*a priori*),

$$\Phi = \{\phi_{kn}\} = \begin{bmatrix} \phi_1(\mathbf{r}_1) & \phi_2(\mathbf{r}_1) & \dots & \phi_K(\mathbf{r}_1) \\ \phi_1(\mathbf{r}_2) & \phi_2(\mathbf{r}_2) & \dots & \phi_K(\mathbf{r}_2) \\ \dots & \dots & \dots & \dots \\ \phi_1(\mathbf{r}_N) & \phi_2(\mathbf{r}_N) & \dots & \phi_K(\mathbf{r}_N) \end{bmatrix}. \quad (\text{A6})$$

This spectral method has been proven effective for the ocean data analysis (Chu et al., 2016). Application of the generalized Fourier series expansion (A3) to the observational points with  $P$  as the total number of observations leads to an algebraic equation

$$\mathbf{A}\mathbf{a} = \mathbf{Q}\mathbf{Y}. \quad (\text{A7})$$

where  $\mathbf{a} = (a_1, a_2, \dots, a_K)$ , is the state vector ( $K$ -dimensional);  $\mathbf{A}$  is a  $P \times K$  matrix;  $\mathbf{Q}$  is a  $P \times P$  square matrix ( $P > K$ );  $\mathbf{Y}$  is a  $P$ -dimensional observation vector, consisting of a signal  $\bar{\mathbf{Y}}$  and a noise  $\mathbf{Y}'$ . Due to the high level of noise contained in the observations, the algebraic Eq. (A7) is ill-posed and needs to be solved by a rotation matrix regularization method (Chu et al., 2004) that provides: (a) stability (robustness) even for noisy data, and (b) the ability to filter out errors with a-priori unknown statistics. Interested readers are referred to Chu et al. (2003a, 2003b, 2004, 2015, 2016).

## References

- Ashok, K., Behera, S., Rao, A.S., Weng, H., Yamagata, T., 2007. El Niño Modoki and its teleconnection. *J. Geophys. Res.* 112, C11007. <http://dx.doi.org/10.1029/2006JC003798>.
- Bond, N.A., Overland, J.E., Spillane, M., Stabeno, P., 2003. Recent shifts in the state of the North Pacific. *Geophys. Res. Lett.* 30 (23), 2183. <http://dx.doi.org/10.1029/2003GL018597>.
- Boyer, T.P., Antonov, J. I., Baranova, O. K., Coleman, C., Garcia, H. E., Grodsky, A., Johnson, D. R., Locarnini, R. A., Mishonov, A. V., O'Brien, T.D., Paver, C.R., Reagan, J.R., Seidov, D., Smolyar, I. V., Zweng, M. M., 2013. World Ocean Database 2013, NOAA Atlas NESDIS 72, Levitus, S., Ed., Mishonov, A., Technical Ed.; Silver Spring, MD, 209 pp., <<http://dx.doi.org/10.7289/V5NZ85MT>>.
- Brink, K.H., Cowles, T.J., 1991. The coastal transition zone program. *J. Geophys. Res.* 96 (C8), 14637–14647.
- Castro, C.G., Chavez, F.P., Collins, C.A., 2001. Role of the California Undercurrent in the export of denitrified waters from the eastern tropical North Pacific. *Glob. Biogeochem. Cycles* 15, 819–830.
- Chhak, K., Di Lorenzo, E., 2007. Decadal variations in the California Current upwelling cells. *Geophys. Res. Lett.* 34, L14604. <http://dx.doi.org/10.1029/2007GL030203>.
- Chhak, K., Di Lorenzo, E., Schneider, N., Cummins, P.F., 2007. Forcing of low-frequency ocean variability in the northeast Pacific. *J. Clim.* 22 (5), 1255–1276.
- Chelton, D.B., 1984. Seasonal variability of alongshore geostrophic velocity off central California. *J. Geophys. Res.* 89, 3473–3486.
- Chu, P.C., Tseng, H.C., Chang, C.P., Chen, J.M., 1997. South China Sea warm pool detected from the Navy's Master Oceanographic Observational Data Set (MOODS). *J. Geophys. Res.* 102, 15761–15771.
- Chu, P.C., Chen, Y.C., Lu, S.H., 1998. Temporal and spatial variabilities of Japan Sea surface temperature and atmospheric forcing. *J. Oceanogr.* 54, 273–284.
- Chu, P.C., Ivanov, L.M., Korzhova, T.P., Margolina, T.M., Melnichenko, O.M., 2003a. Analysis of sparse and noisy ocean current data using flow decomposition. Part 1: theory. *J. Atmos. Ocean. Technol.* 20, 478–491.
- Chu, P.C., Ivanov, L.M., Korzhova, T.P., Margolina, T.M., Melnichenko, O.M., 2003b. Analysis of sparse and noisy ocean current data using flow decomposition. Part 2: application to Eulerian and Lagrangian data. *J. Atmos. Ocean. Technol.* 20, 492–512.
- Chu, P.C., Ivanov, L.M., Margolina, T.M., 2004. Rotation method for reconstructing process and field from imperfect data. *Int. J. Bifurc. Chaos* 14, 2991–2997.
- Chu, P.C., Tokmakian, R.T., Fan, C.W., Sun, C.L., 2015. Optimal spectral decomposition (OSD) for ocean data assimilation. *J. Atmos. Ocean. Technol.* 32, 828–841.
- Chu, P.C., Fan, C.W., Margolina, T., 2016. Ocean spectral data assimilation without background error covariance matrix. *Ocean Dyn.* 66, 1143–1163.
- Chu, P.C., Fan, C.W., 2017. Synoptic monthly gridded global and regional four dimensional WOD and GTSP (T, S, u, v) fields with the optimal spectral decomposition (OSD) and P-vector methods. *Geosci. Data J.* 4 (2), 50–71.
- Collins, C.A., Paquette, R.G., Ramp, S.R., 1996. Annual Variability of Ocean Currents at 350m Depth Over the Continental Slope off Point Sur, California 37. California Cooperative Oceanic Fisheries Investigations, La Jolla, pp. 257–263 (CalCOFI Report).
- Collins, C.A., Garfield, N., Rago, T.A., Risermiller, F.W., Carter, E., 2000. Mean structure of the inshore countercurrent and California Undercurrent off Point Sur, California. *Deep Sea Res. Part II* 47, 765–782.
- De Szoek, R.A., 2000. Equations of motion using thermodynamic coordinates. *J. Phys. Oceanogr.* 30, 2814–2829.
- Hickey, B., 1979. The California Current system- hypotheses and facts. *Prog. Oceanogr.* 8, 191–279.
- Jacox, M.G., Hazen, E.L., Zaba, K.D., Rudnick, D.L., Edwards, C.A., Moore, A.M., Bograd, S.J., 2016. Impacts of the 2015–2016 El Niño on the California Current System: early

- assessment and comparison to past events. *Geophys. Res. Lett.* 43, 7072–7080. <http://dx.doi.org/10.1002/2016GL069716>.
- Kawabe, M., Fujio, S., 2010. Pacific ocean circulation based on observation. *J. Oceanogr.* 66, 389–403.
- Kosro, P.M., 1987. Structure of the coastal current field off northern California during the Coastal Ocean Dynamics Experiment. *J. Geophys. Res.* 92, 1637–1654.
- Kosro, P.M., Huyer, A., 1986. CTD and velocity surveys of seaward jets off northern California, July 1981 and 1982. *J. Geophys. Res.* 91, 7680–7690.
- Kosro, P.M., Huyer, A., Ramp, S.R., Smith, R.L., Chavez, F.P., Cowles, T.J., Abbott, M.R., Strub, P.T., Barber, R.T., Jessen, P.F., Small, L.F., 1991. The structure of the transition zone between coastal waters and the open ocean off northern California, winter and spring 1987. *J. Geophys. Res.* 96, 14707–14730.
- Ladd, M.D., Wilson, G.R., 1993. Frequency resolution properties of the wavelet transform for detecting harmonically related narrowband signal. 1993 IEEE International Conference on Acoustics, Speech, and Signal Processing, <<http://dx.doi.org/10.1109/ICASSP.1993.913684>>, iv-420–iv-423.
- Lorenz, E.N., 1956. Empirical Orthogonal Functions and Statistical Weather Prediction. M.I.T., Cambridge, MA, pp. 48 (Sci. Rep. No. 1, Statistical Forecasting Project).
- Lynn, R.J., Simpson, J.J., 1987. The California current system: the seasonal variability of its physical characteristics. *J. Geophys. Res.* 92, 12,947–12,966.
- Mallat, S.G., 1989. A theory for multiresolution signal decomposition: the wavelet representation. *IEEE Trans. Pattern Anal. Mach. Intell.* 11, 674–693.
- Montgomery, R.B., 1937. A suggested method for representing gradient flow in isentropic surfaces. *Bull. Am. Meteorol. Soc.* 18, 210–212.
- Neelin, J.D., Jin, F., Syu, H., 2000. Variations in ENSO phase locking. *J. Clim.* 13, 2570–2590.
- Paduan, J.D., Niiler, P.P., 1990. A Lagrangian description of motion in northern California coastal transition filaments. *J. Geophys. Res.* 95, 18095–18109.
- Pierce, D.W., Barnett, T.P., Schneider, N., Saravanan, R., Dommenges, D., Latif, M., 2001. The role of ocean dynamics in producing decadal climate variability in the North Pacific. *Clim. Dyn.* 18, 51–70.
- Reid, J.L., Roden, G.I., Wyllie, J.G., 1958. Studies of the California Current System. California Cooperative Oceanic Fisheries Investigations, La Jolla, pp. 27–56 (CalCOFI Report, 7/1/56- 1/1/58).
- Sciremammano, F., 1979. A suggestion for the presentation of correlations and their significance levels. *J. Phys. Oceanogr.* 9, 1273–1276.
- Steger, J.M., Collins, C.A., Chu, P.C., 1998. Circulation in the Archipelago de Colon (Galapagos Islands), November 1993. *Deep Sea Res. Part-II* 45, 1093–1114.
- Taylor, S.V., Cayan, D.R., Graham, N.E., Georgakakos, K.P., 2008. Northerly surface winds over the eastern North Pacific Ocean in spring and summer. *J. Geophys. Res.* 113, D02110. <http://dx.doi.org/10.1029/2006JD008053>.
- Torrence, C., Compo, G.P., 1998. A practical guide to wavelet analysis. *Bull. Am. Meteorol. Soc.* 79, 61–78.
- Weng, H., Ashok, S.K., Behera, S., Rao, A., Yamagata, T., 2007. Impacts of recent El Niño Modoki on dry/wet conditions in the Pacific Rim during boreal summer. *Clim. Dyn.* 29, 113–129.
- Wilks, D.S., 2005. *Statistical Methods in the Atmospheric Sciences: An Introduction*. Elsevier Science (ProQuest Ebook Central). <<https://ebookcentral.proquest.com/lib/ebook-nps/detail.action?docID=269991>>.
- Wolter, K., Timlin, M.S., 2011. El Niño/Southern Oscillation behavior since 1871 as diagnosed in an extended multivariate ENSO index. *Int. J. Climatol.* 31, 1074–1087.
- Wyllie, J. 1966. Geostrophic flow of the California Current at the surface and at 200 meters. California Cooperative Oceanic Fisheries Investigations La Jolla Atlas 4.
- Yamanaka, G., Kitamura, Y., Endoh, M., 1998. Formation of North Pacific Intermediate Water in Meteorological Research Institute ocean general circulation model: 2. Transient tracer experiments. *J. Geophys. Res.* 103, 30905–30921. <http://dx.doi.org/10.1029/1998JC900006>.
- You, Y., 2003. The pathway and circulation of North Pacific Intermediate Water. *Geophys. Res. Lett.* 30, 2291. <http://dx.doi.org/10.1029/2003GL018561>.
- Zhang, Y., Wallace, J.M., Battisti, D.S., 1997. ENSO-like interdecadal variability: 1900–93. *J. Clim.* 10, 1004–1020.